Ramakrishna Mission Residential College (Autonomous)
Kolkata 700103, WB, India

Collaborative research in coordination chemistry of organic radicals

Number 9

Institute 1: Ramakrishna Mission Residential College (Autonomous)

Concerned Faculty: Dr. Prasanta Ghosh, Dept of Chemistry

&

Institute 2: **Max-Planck-Institut für Chemische Energiekonversion**

Stiftstrasse 34 - 36 / D - 45470 Mülheim an der Ruhr

Concerned Scientist: Dr Thomas Weyhermüller

Period of Investigation: 02-02-2016 to 27-10-2016

Project: Arylamino radical complexes of heavier transition elements

Output: The result was published in a journal of international repute

Publication: Arylamino radical complexes of ruthenium and osmium: dual radical counter in a molecule

Sachinath Bera, Suvendu Maity, Thomas Weyhermüller and Prasanta Ghosh*

Dalton Trans., 2016, *45*, 19428-19440

Dr. Prasanta Ghosh

Dr Thomas Weyhermüller

Dalton Transactions

PAPER

Cite this: *Dalton Trans.*, 2016, **45**, 19428

Arylamino radical complexes of ruthenium and osmium: dual radical counter in a molecule†

Sachinath Bera,[a] Suvendu Maity,[a] Thomas Weyhermüller[b] and Prasanta Ghosh*[a]

Radical and non-radical ruthenium and osmium complexes of 1-amino-9,10-anthraquinone ($AqNH_2$), which is defined as a molecule of dual radical counter, are disclosed. 1-Amido-9,10-anthraquinone ($AqNH^-$) complexes of the types *trans*-$[Ru^{II}(AqNH^-)(PPh_3)_2(CO)Cl]$ (**1**), *trans*-$[Os^{II}(AqNH^-)(PPh_3)_2(CO)Br]$ (**2**) and *trans*-$[Ru^{III}(AqNH^-)(PPh_3)_2Cl_2]$ (**3**) were isolated. $AqNH^-$ of **1–3** is redox active and undergoes oxidation reversibly at +(0.05–0.35) V to the 1-amino-9,10-anthraquinone radical ($AqNH^\bullet$) and reduction at -(0.86–1.60) V to the 1-amido-9,10-anthrasemiquinonate anion radical ($Aq^{NH}SQ^{\bullet 2-}$). The reaction of **2** with I_2 in CH_2Cl_2 afforded a crystalline $AqNH^\bullet$ complex of the type *trans*-$[Os^{II}(AqNH^\bullet)(PPh_3)_2(CO)Br]^+I_5^-\cdot\frac{1}{2}I_2$ ($\mathbf{2}^+I_5^-\cdot\frac{1}{2}I_2$). $AqNH^\bullet$ and $Aq^{NH}SQ^{\bullet 2-}$ complexes of the types *trans*-$[Ru^{II}(AqNH^\bullet)(PPh_3)_2(CO)Cl]^+$ ($\mathbf{1}^+$), *trans*-$[Ru^{III}(AqNH^\bullet)(PPh_3)_2Cl_2]^+$ ($\mathbf{3}^+$), *trans*-$[Ru^{II}(Aq^{NH}SQ^{\bullet 2-})(PPh_3)_2(CO)Cl]^-$ ($\mathbf{1}^-$) and *trans*-$[Os^{II}(Aq^{NH}SQ^{\bullet 2-})(PPh_3)_2(CO)Br]^-$ ($\mathbf{2}^-$) were generated chemically/electrochemically in solution. The electronic states of the complexes were authenticated by single crystal X-ray structure determinations of **1**, **2**·5/4 toluene, **3** and $\mathbf{2}^+I_5^-\cdot\frac{1}{2}I_2$, EPR spectroscopy and density functional theory (DFT) calculations. $AqNH^\bullet$ instigates a 2c–3e p_π–d_π interaction and the $Os^{II} - NH^\bullet_{Aq}$ length in $\mathbf{2}^+I_5^-\cdot\frac{1}{2}I_2$, 1.978(5) Å, is relatively shorter than the Os^{II}–NH_{Aq}^- length, 2.037(2) Å, while the Aq–$NH^\bullet$ bond, 1.365(8) Å, is longer than the Aq–NH^- bond, 1.328(3) Å. DFT calculations predicted that the atomic spin is delocalized over the ligand backbone ($\mathbf{1}^+$, 56%) particularly in one of the p-orbitals of the nitrogen and the metal atoms of the $\mathbf{1}^+$ and $\mathbf{2}^+$ ions, while the spin is dominantly localized on the anthraquinone fragment of the $\mathbf{1}^-$ and $\mathbf{2}^-$ ions. TD DFT calculations were employed to elucidate the origins of the lower energy absorption bands of the neutral complexes. Hypsochromic shifts of the UV-vis-NIR absorption maximum during $\mathbf{1}\rightarrow\mathbf{1}^+$, $\mathbf{2}\rightarrow\mathbf{2}^+$ and $\mathbf{3}\rightarrow\mathbf{3}^+$ conversions were recorded by spectroelectrochemical measurements.

Received 26th September 2016,
Accepted 4th November 2016

DOI: 10.1039/c6dt03728c

www.rsc.org/dalton

Introduction

The tyrosyl radical plays a crucial role in several redox reactions in biology.[1] The reactivities and the properties of the aryloxyl radicals ($ArO^\bullet$)[2] have been explored in different aspects of chemistry. However, the parallel chemistry of the isoelectronic reactive anilino radicals ($ArNH^\bullet$) is limited, and broadly, transition metal nitrogen centered radical complexes are rare.[3] The participation of the nitrogen centered radical intermediate in metallo-enzymes to perform different organic reactions is documented in several instances.[4] The types of arylamino radical complexes documented so far are listed in Chart 1. Wieghardt[5] authenticated the formation of $ArNH^\bullet$ radicals coordinated to cobalt(II) and manganese(IV) ions, of type **A** in Chart 1, while Tanaka[6] detected an $ArNH^\bullet$ complex of

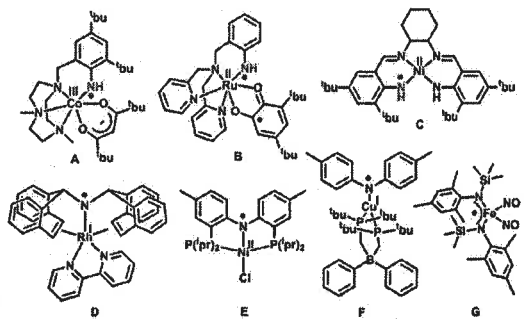

Chart 1 Reported anilino (A–C) and aminyl (D–G) radical complexes of transition metal ions.

[a]*Department of Chemistry, R. K. Mission Residential College, Narendrapur, Kolkata-103, India. E-mail: ghosp@pghosh.in*

[b]*Max-Planck-Institut für Chemische Energiekonversion, Stiftstrasse 34-36, D-45470 Mülheim, Germany*

†Electronic supplementary information (ESI) available: X-ray crystallographic CIF files for the **1**, **2**·5/4 toluene, **3** and $\mathbf{2}^+I_5^-\cdot1/2I_2$; calculated bond parameters; photoactive orbitals; gas phase optimized coordinates of $AqNH^\bullet$, $AqNH^-$, $\mathbf{1}^{Me}$, $\mathbf{1}^{Me+}$, $\mathbf{1}^{Me-}$, $\mathbf{2}^{Me}$, $\mathbf{2}^{Me+}$ $\mathbf{2}^{Me-}$, $\mathbf{3}^{Me}$ and $\mathbf{3}^{Me-}$; excitation energies, oscillator strengths, transition types and dominant contributions of UV-vis-NIR absorption bands from TD DFT calculations. CCDC 1447861–1447863, 1447878 and 1490059. For ESI and crystallographic data in CIF or other electronic format see DOI: 10.1039/c6dt03728c

ruthenium(II) of type **B**. Thomas[7] was successful in isolating the crystalline complexes of $ArNH^{\bullet}$ coordinated to nickel(II) and cobalt(II) ions of type **C**, which were characterized by single crystal X-ray bond parameters. The aminyl radical ($R_2N^{\bullet}$) complexes of transition metal ions are also inadequate. Grützmacher[8] disclosed the chemistry of $R_2N^{\bullet}$ by isolating crystalline complexes of rhodium(I) of type **D**. Mindiola[9a] isolated an $R_2N^{\bullet}$ complex of nickel(II) of type **E**, while Peters[9b] isolated an $R_2N^{\bullet}$ complex of copper(I) of type **F**. Recently, an $R_2N^{\bullet}$ radical of type **G**, stabilized by $[Fe(NO)_2]$, was reported by Hsu and Liaw.[9c] **D–G** were substantiated precisely by single crystal X-ray bond parameters, different spectroscopy and quantum chemical calculations.

The literature reveals that the isolated nitrogen centered radical complexes of transition metal ions are limited in scope, and the generation of these reactive $ArNH^{\bullet}$ and $R_2N^{\bullet}$ intermediates to assign their benchmark features is a challenge in chemistry. In this study, the issue is addressed, isolating $ArNH^{-}$ and $ArNH^{\bullet}$ complexes of ruthenium(II/III) and osmium(II) ions using triphenyl phosphine, carbonyls and halides as co-ligands. The arylamine used to explore this radical chemistry is 1-amino-9,10-anthraquinone ($AqNH_2$), that upon oxidation produces the 1-amino-9,10-anthraquinone radical ($AqNH^{\bullet}$) and upon reduction generates the 1-amido-9,10-anthrasemiquinonate anion radical ($Aq^{NH}SQ^{\bullet 2-}$), a *p*-aryl semiquinonate anion radical. It is justified to mention that the transition metal complexes of the *p*-arylsemiquinonate anion radical are remarkably less explored.[10a–c]

In this study, the $AqNH^{\bullet}$ state was successfully authenticated by the single crystal X-ray bond parameters. As both $AqNH^{\bullet}$ and $Aq^{NH}SQ^{\bullet 2-}$ radicals are achieved from 1-amido-9,10-anthraquinone ($AqNH^{-}$) as shown in Scheme 1, the redox non-innocent $AqNH_2$ is defined as a dual radical counter in a molecule. The coordination complexes of these types of molecules are worthy, as both oxidized and reduced states of these complexes bear an organic radical and are expected to be more reactive. In the vast coordination chemistry, such a metallo-organic fragment, although it appears to be a significant entity to promote redox reactions, has not been explored earnestly.

The $AqNH^{-}$, $AqNH^{\bullet}$ and $Aq^{NH}SQ^{\bullet 2-}$ complexes presented in this article are illustrated in Chart 2. *trans*-$[Ru^{II}(AqNH^{-})(PPh_3)_2(CO)Cl]$ (**1**), *trans*-$[Os^{II}(AqNH^{-})(PPh_3)_2(CO)Br]$ (**2**), *trans*-$[Ru^{III}(AqNH^{-})(PPh_3)_2Cl_2]$ (**3**) and *trans*-$[Os^{II}(AqNH^{\bullet})(PPh_3)_2(CO)Br]^{+}I_5^{-}\cdot\frac{1}{2}I_2$ ($2^{+}I_5^{-}\cdot\frac{1}{2}I_2$) were isolated as crystalline materials which were analyzed by different spectroscopy and single crystal X-ray structure determinations. *trans*-$[Ru^{II}(AqNH^{\bullet})(PPh_3)_2(CO)Cl]^{+}$ (1^{+}), *trans*-$[Ru^{II}(Aq^{NH}SQ^{\bullet 2-})(PPh_3)_2(CO)Cl]^{-}$ (1^{-}), *trans*-$[Os^{II}(Aq^{NH}SQ^{\bullet 2-})(PPh_3)_2(CO)Br]^{-}$ (2^{-}), *trans*-$[Ru^{III}(AqNH^{\bullet})(PPh_3)_2Cl_2]^{+}$ (3^{+}) and *trans*-$[Ru^{III}(Aq^{NH}SQ^{\bullet 2-})(PPh_3)_2Cl_2]^{-}$ (3^{-}) ions were chemically/electrochemically generated in solution and were characterized by spectroelectrochemical measurements and variable temperature EPR spectra. In conjunction with the experimental bond parameters and spectral data, density functional theory (DFT) calculations were employed to support in elucidating the electronic structures of these complexes.

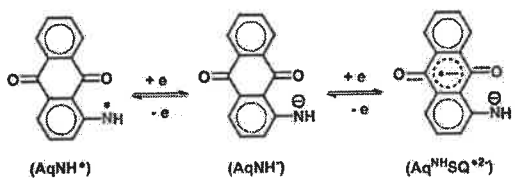

Scheme 1 $AqNH^{\bullet}$ and $Aq^{NH}SQ^{\bullet 2-}$ radical states achieved from $AqNH^{-}$.

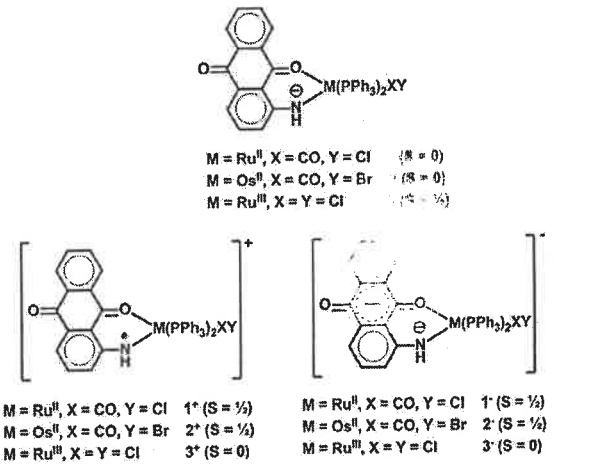

Chart 2 $AqNH^{-}$, $AqNH^{\bullet}$ and $Aq^{NH}SQ^{\bullet 2-}$ complexes of ruthenium(II/III) and osmium(II) ions reported in this article.

Experimental section

Materials and physical measurements

1-Amino-9,10-anthraquinone ($AqNH_2$) was purchased from Sigma-Aldrich and other reagents or analytical-grade materials were obtained from commercial suppliers and used without further purification. The precursors $[Ru^{II}(PPh_3)_3(CO)(H)Cl]$, $[Ru^{II}(PPh_3)_3Cl_2]$ and $[Os^{II}(PPh_3)_3(CO)(H)Br]$ were prepared by reported procedures.[11] Spectroscopic-grade solvents were used for spectroscopic and electrochemical measurements. The C, H, and N contents of the compounds were obtained from a Perkin-Elmer 2400 Series II elemental analyzer. The elemental analyses were performed after evaporating the solvents under high vacuum. Infrared spectra of the samples were measured from 4000 to 400 cm^{-1} with KBr pellets at 295 K on a PerkinElmer Spectrum RX 1 Fourier transform infrared (FT-IR) spectrophotometer. ^1H NMR spectra in $CDCl_3$ were recorded on a Bruker DPX 300 MHz spectrometer. Electrospray ionization (ESI) mass spectra were recorded on a micro mass Q-TOF mass spectrometer. Electronic absorption spectra of the solutions of the complexes were recorded on a PerkinElmer Lambda 750 spectrophotometer over the range of 3300–175 nm. The X-band EPR spectra were recorded on a Magnettech GmbH MiniScope MS400 spectrometer (equipped

with a temperature controller TC H03), where the microwave frequency was measured with an FC400 frequency counter. The EPR spectra were simulated using EasySpin software. The electro-analytical instrument, BASi Epsilon-EC, was used for cyclic voltammetric experiments in CH_2Cl_2 containing 0.2 M tetrabutylammonium hexafluorophosphate as the supporting electrolyte. The BASi platinum working electrode, platinum auxiliary electrode, and Ag/AgCl reference electrode were used for the measurements. The redox potential data were referenced to the ferrocenium/ferrocene, Fc^+/Fc, couple. The BASi SEC-C thin-layer quartz glass spectro-electrochemical cell kit (light path length of 1 mm) with a platinum gauze working electrode and a SEC-C platinum counter electrode were used for the spectro-electrochemistry measurements.

Syntheses

***trans*-[Ru^{II}($AqNH^-$)(PPh_3)$_2$(CO)Cl] (1).** To a solution of $AqNH_2$ (23 mg, 0.1 mmol) in dry toluene (15 ml) [$Ru^{II}(PPh_3)_3$(CO)(H)Cl] (100 mg, 0.1 mmol) was added and the mixture was refluxed for 1 h in air. Upon cooling at 295 K, a green crystalline material of **1** separated out. Yield: 82 mg (86% with respect to ruthenium). Single crystals for X-ray diffraction were grown by diffusion of *n*-hexane to a CH_2Cl_2 solution of **1**. Mass spectral data [ESI, positive ion, CH_2Cl_2]: *m/z* 586 for [**1**-(PPh_3 + Cl + CO)]$^+$. ^{1}H NMR ($CDCl_3$, 300 MHz): δ(ppm) 8.36 (d, 2H), 8.02 (d, 2H), 7.75–7.71 (m, 13H), 7.55 (t, 1H), 7.26–7.20 (m, 17H), 6.92 (d, 2H), 4.32 (s, 1H). Anal. Calcd (%) for $C_{51}H_{38}ClNO_3P_2Ru$; C, 67.22; H, 4.20; N, 1.54. Found: C, 66.96; H, 4.18; N, 1.54. IR/cm^{-1} (KBr): ν 3350 (m, –NH), 3046 (w), 1940 (s), 1657 (s), 1588 (m), 1437 (s), 1298 (s), 1360 (m), 1091 (s), 1022 (m), 794 (m), 690 (s), 518 (s).

***trans*-[Os^{II}($AqNH^-$)(PPh_3)$_2$(CO)Br]·5/4 toluene (2·5/4 toluene).** To a solution of $AqNH_2$ (23 mg, 0.1 mmol) in dry toluene (15 ml) [$Os^{II}(PPh_3)_3$(CO)(H)Br] (100 mg, 0.1 mmol) was added. The mixture was refluxed for 1 h in air and the resulting solution was allowed to evaporate slowly under air at 295 K. After a few days, dark green single crystals of **2**·5/4 toluene separated out, which were filtered and dried in air. Yield: 78 mg (80% with respect to osmium). Single crystals for X-ray diffraction and all spectroscopic and electrochemical measurements were performed using this product. Mass spectral data [ESI, positive ion, CH_2Cl_2]: *m/z* 1045 for [**2**]$^+$. ^{1}H NMR ($CDCl_3$, 300 MHz): δ(ppm) 8.20 (d, 2H), 8.02 (d, 2H), 7.70–7.58 (m, 13H), 7.55 (t, 1H), 7.26–7.19 (m, 17H), 6.45 (d, 2H), 4.12 (s, 1H). Anal. Calcd (%) for $C_{51}H_{38}BrNO_3P_2Os$; C, 58.62; H, 3.67; N, 1.34. Found: C, 58.26; H, 3.65; N, 1.34. IR/cm^{-1} (KBr): ν 3300 (s, –NH), 3049 (m), 1926 (s), 1635 (s), 1584 (s), 1507 (s) 1481 (s), 1300 (s), 1091 (s), 1023 (m), 802 (m), 726 (m), 693 (s), 516 (s).

***trans*-[Ru^{III}($AqNH^-$)(PPh_3)$_2$Cl$_2$] (3).** To a solution of $AqNH_2$ (23 mg, 0.1 mmol) in dry ethanol (20 ml) [$Ru^{II}(PPh_3)_3Cl_2$] (100 mg, 0.1 mmol) was added and the mixture was refluxed for 1 h in air, and crystalline material of **3** separated out. Yield: 80 mg (87% with respect to ruthenium). Single crystals for X-ray diffraction were grown by diffusion of *n*-hexane to a CH_2Cl_2 solution of **3**. Mass spectral data [ESI, positive ion, CH_2Cl_2]: *m/z* 939.6 for [3 + Na]$^+$ and 883.6 for [3 – Cl]$^+$. Anal. Calcd (%) for $C_{50}H_{38}Cl_2NO_2P_2Ru$; C, 65.36; H, 4.17; N, 1.52. Found: C, 65.06; H, 4.16; N, 1.52. IR/cm^{-1} (KBr): ν 3310 (m, –NH), 3051 (m), 1657 (s), 1584 (s), 1481 (s), 1433 (s), 1409 (s), 1268 (s), 1166 (s), 1090 (s), 1021 (m), 747 (m), 693 (s), 519 (s).

***trans*-[Os^{II}($AqNH^{\bullet}$)(PPh_3)$_2$(CO)Br]$^+I_5^-\cdot\frac{1}{2}I_2$ ($2^+I_5^-\cdot\frac{1}{2}I_2$).** To a solution of **2** (50 mg, 0.05 mmol) in dry dichloromethane (10 ml) in a long glass tube, iodine solution in hexane (50 mg, 0.2 mmol) was allowed to diffuse. After a few days, single crystals of $2^+I_5^-\cdot\frac{1}{2}I_2$ separated out, which were collected for further analyses. Yield: 50 mg (57% with respect to osmium). Mass spectral data [ESI, positive ion, CH_2Cl_2]: *m/z* 1045 for [**2**]$^+$. Anal. Calcd (%) for $C_{51}H_{38}BrI_6NO_3P_2Os$; C, 33.91; H, 2.12; N, 0.78. Found: C, 33.76; H, 2.12; N, 0.78. IR/cm^{-1} (KBr): ν 3434 (br, –NH), 3049 (m), 1968 (s), 1664 (s), 1584 (s), 1481 (m), 1433 (s), 1367 (m), 1291 (s), 1257 (m), 1091 (m), 693 (s), 518 (s).

Complexes 1^+, 3^+ and $[1\text{–}2]^-$. These complexes were not isolated in this investigation. However, they were generated by coulometric experiments in CH_2Cl_2 at 295 K for spectroelectrochemical measurements and EPR spectra. Complexes 1^+ and 3^+ were generated upon oxidation of **1** and **3**, respectively, at +0.34 and +0.60 V with respect to the Fc^+/Fc couple, whereas 1^- and 2^- were produced upon reduction of **1** and **2**, respectively, at –1.80 and –1.70 V, respectively. $[1\text{–}2]^-$ were also generated chemically in CH_2Cl_2 using an equivalent amount of cobaltocene as a reducing agent.

Single-crystal X-ray structure determinations of the complexes (CCDC: 1447861–63, 1447878 and 1490059)

Dark single crystals of **1**, **2**·5/4 toluene, **3** and $2^+I_5^-\cdot\frac{1}{2}I_2$ were picked up with nylon loops and mounted on a Bruker APEX-II CCD and Bruker AXS D8 QUEST ECO diffractometer equipped with a Mo-target rotating-anode X-ray source and a graphite monochromator (Mo Kα, λ = 0.71073 Å). Final cell constants were obtained from least-squares fits of all measured reflections. Intensity data were corrected for absorption using intensities of redundant reflections. The structures were readily solved by direct methods and subsequent difference Fourier techniques. The Siemens SHELXS-97 [12a] software package was used for the solution, SHELXL-97 [12b] was used for the refinement, and XS. Ver. 2013/1,[12c] XT. Ver. 2014/4 [12d] and XL. Ver. 2014/7 [12e] were used for the structure solution and refinement. All non-hydrogen atoms were refined anisotropically. Hydrogen atoms were placed at the calculated positions and refined as riding atoms with isotropic displacement parameters.

The checkcif of $2^+I_5^-\cdot\frac{1}{2}I_2$ records an 'A' label error as the structure suffers from slight disorder of the complex cation and the I_5^- anionic unit. Five relatively small residual density peaks (2.56–2.02 e A^{-3}) are located in close vicinity (0.42–0.96 A) to the osmium and iodine atoms, which are common to heavier atoms with diffuse orbitals.

Density functional theory (DFT) calculations

All calculations reported in this article were done with the Gaussian 03W [13] program package supported by GaussView

4.1. The DFT[14] and time-dependent (TD) DFT[15] calculations were performed at the level of the Becke three parameter hybrid functional with the nonlocal correlation functional of Lee–Yang–Parr (B3LYP).[16] Gas-phase geometries of $AqNH^-$, *trans*-$[Ru^{II}(AqNH^-)(PMe_3)_2(CO)Cl]$ (1^{Me}), *trans*-$[Os^{II}(AqNH^-)(PMe_3)_2(CO)Br]$ (2^{Me}) and *trans*-$[Ru^{III}(AqNH^-)(PMe_3)_2Cl_2]^+$ (3^{Me+}) were optimized with the singlet spin state. Gas-phase geometries of $AqNH^\bullet$, *trans*-$[Ru^{II}(AqNH^\bullet)(PMe_3)_2(CO)Cl]^+$ (1^{Me+}), *trans*-$[Os^{II}(AqNH^\bullet)(PMe_3)_2(CO)Br]^+$ (2^{Me+}), *trans*-$[Ru^{II}(Aq^{NH}SQ^{\bullet 2-})(PMe_3)_2(CO)Cl]^-$ (1^{Mc-}), *trans*-$[Os^{II}(Aq^{NH}SQ^{\bullet 2-})(PMe_3)_2(CO)Br]^-$ (2^{Me-}) and *trans*-$[Ru^{III}(AqNH^-)(PMe_3)_2Cl_2]$ (3^{Me}) were optimized with the doublet spin state, using Pulay's Direct Inversion[17] in the Iterative Subspace (DIIS), a "tight" convergent self consistent field procedure[18] ignoring symmetry. In all calculations, a LANL2DZ basis set along with the corresponding effective core potential (ECP) was used for the ruthenium ion.[19] The ground state energies and the atomic spin of **1**, **2** and 2^+ in CH_2Cl_2 were calculated using crystallographic coordinates. A valence double-ζ basis set, 6-31G for H, was used.[20] For C, N, P, Cl, and Br non-hydrogen atoms, a valence double-ζ basis set[21] with diffuse and polarization functions, 6-31+G*, was employed for all calculations. The 60 lowest singlet excitation energies on each of the optimized geometries of $AqNH^-$, 1^{Me} and 2^{Me} were elucidated by TD DFT calculations. The natures of transitions were calculated by adding the probability of the same type among α and β molecular orbitals.

$$[Ru^{II}(PPh_3)_3(H)(CO)Cl] + AqNH_2 \xrightarrow{-(H^+ + H^-)} 1 + PPh_3$$

$$[Os^{II}(PPh_3)_3(H)(CO)Br] + AqNH_2 \xrightarrow{-(H^+ + H^-)} 2 + PPh_3$$

$$[Ru^{II}(PPh_3)_3Cl_2] + AqNH_2 \xrightarrow{-H^+} 3 + PPh_3$$

$$2 + 3I_2 \longrightarrow 2^+I_5^-\cdot\tfrac{1}{2}I_2$$

Chart 3

Results and discussion

Syntheses and characterization

Reactions of 1-amino-9,10-anthraquinone ($AqNH_2$) with the hydride precursors $[Ru^{II}(PPh_3)_3(CO)(H)Cl]$ and $[Os^{II}(PPh_3)_3(CO)(H)Br]$ in boiling toluene afforded diamagnetic $AqNH^-$ complexes of the types *trans*-$[Ru^{II}(AqNH^-)(PPh_3)_2(CO)Cl]$ (**1**) and *trans*-$[Os^{II}(AqNH^-)(PPh_3)_2(CO)Br]$ (**2**) in good yields. Similarly, the reaction of $AqNH_2$ with a non-halide precursor, $[Ru^{II}(PPh_3)_3Cl_2]$, yielded a paramagnetic ruthenium(III) complex of the type *trans*-$[Ru^{III}(AqNH^-)(PPh_3)_2Cl_2]$ (**3**). *trans*-$[Os^{II}(AqNH^\bullet)(PPh_3)_2(CO)Br]^+I_5^-\cdot\frac{1}{2}I_2$ ($2^+I_5^-\cdot\frac{1}{2}I_2$) was isolated by reacting **2** with iodine in a CH_2Cl_2–hexane mixture at 295 K. The stoichiometries of the reactants and the products are given in Chart 3. *trans*-$[Ru^{II}(AqNH^\bullet)(PPh_3)_2(CO)Cl]^+$ (1^+) and *trans*-$[Ru^{III}(AqNH^\bullet)(PPh_3)_2Cl_2]^+$ (3^+) were generated by constant potential coulometric experiments using tetrabutylammonium hexafluorophosphate as an electrolyte, while *trans*-$[Ru^{II}(Aq^{NH}SQ^{\bullet 2-})(PPh_3)_2(CO)Cl]^-$ (1^-) and *trans*-$[Os^{II}(Aq^{NH}SQ^{\bullet 2-})(PPh_3)_2(CO)Br]^-$ (2^-) were generated by reducing **1** and **2** with cobaltocene in CH_2Cl_2 as well as by constant potential coulometric experiments at 295 K. The *trans* abbreviations of the complexes are because of the two PPh_3 ligands which lie *trans* to each other. Details of the syntheses and the analytical and spectral data of **1**–**3** and $2^+I_5^-\cdot\frac{1}{2}I_2$ are summarized in the Experimental section.

The IR spectrum of $2^+I_5^-\cdot\frac{1}{2}I_2$, which is a 17e species, is notably different from those of **1** and **2**. The N–H stretching frequencies of **1** and **2** are considerably higher (3350 and 3359 cm^{-1}) than that of $2^+I_5^-\cdot\frac{1}{2}I_2$ (3256 cm^{-1}). The N–H stretching vibration of **3** appears at 3265 cm^{-1}. The bond orders of C=O (non-coordinated) and C≡O of $2^+I_5^-\cdot\frac{1}{2}I_2$ are higher than those of the 18e species, **1** and **2**. The $\nu_{C=O}$ and $\nu_{C\equiv O}$ of **2** at 1652 and 1920 cm^{-1} respectively are blue shifted to 1666 and 1967 cm^{-1} respectively in $2^+I_5^-\cdot\frac{1}{2}I_2$. The corresponding $\nu_{C=O}$ and $\nu_{C\equiv O}$ of **1** are observed at 1657 and 1940 cm^{-1}.

Table 1 Selected experimental bond lengths (Å) of **1**, **2**·5/4 toluene, **3** and $2^+I_5^-\cdot\frac{1}{2}I_2$

	1	2·5/4 toluene	3	$2^+I_5^-\cdot\frac{1}{2}I_2$	
Bonds	100 K	100 K	296 K	135 K	295 K
$M-NH_{Aq}^-/NH_{Aq}^\bullet$	2.031(2)	2.037(2)	1.972(2)	1.978(5)	2.017(11)
M–O	2.090(2)	2.094(2)	2.015(2)	2.096(4)	2.085(7)
M–CO	1.833(2)	1.844(3)		1.915(6)	1.910(12)
M–PPh_3	2.405(1)	2.383(1)	2.444(1)	2.426(2)	2.432(3)
	2.423(1)	2.408(1)	2.424(1)	2.430(2)	2.444(3)
M–X	2.423(1)	2.583(1)	2.343(1)/2.389(1)	2.527(2)	2.526(2)
Aq–NH	1.323(2)	1.328(3)	1.329(3)	1.363(5)	1.366(15)
C2–C3	1.443(2)	1.447(4)	1.429(3)	1.416(7)	1.439(17)
C3–C4	1.362(2)	1.355(4)	1.362(4)	1.377(10)	1.36(2)
C4–C5	1.416(2)	1.419(4)	1.390(4)	1.392(11)	1.38(2)
C5–C6	1.378(2)	1.372(4)	1.368(3)	1.383(10)	1.391(19)
C6–C15	1.442(2)	1.454(4)	1.436(3)	1.419(9)	1.418(18)
C2–C15	1.449(2)	1.455(4)	1.438(3)	1.425(9)	1.413(17)
C14–C15	1.419(2)	1.418(4)	1.420(3)	1.442(9)	1.457(16)
C14–O16	1.274(2)	1.286(3)	1.272(2)	1.263(7)	1.248(13)
C7–O17	1.228(2)	1.235(3)	1.224(3)	1.213(9)	1.195(17)

Assignment of the electronic states of the complexes

The single crystal X-ray bond parameters, redox activity, EPR spectroscopy and the atomic spin density were used to elucidate the electronic structures of the complexes.

X-ray crystallography

The single crystal X-ray structures of **1**, **2**·5/4 toluene, **3** and $2^{+}I_5^{-}\cdot\frac{1}{2}I_2$ are reported. The crystallographic data of these complexes are summarized in Table S1,† and selected bond lengths are listed in Table 1. **1** and **2**·5/4 toluene crystallize in the $P2_1/c$ space group. The molecular geometries in crystals and the atom labeling schemes are illustrated in Fig. 1(a) and (b). The Ru^{II}–NH_{Aq}^{-} and Os^{II}–NH_{Aq}^{-} lengths are 2.031(2) and 2.037(2) Å, while the Ru^{II}–O and Os^{II}–O distances are 2.090(2) and 2.094(2) Å respectively. The Ru^{II}–CO, Ru^{II}–PPh_3, Os^{II}–CO and Os^{II}–PPh_3 lengths correlate well to those reported in similar types of ruthenium(II) and osmium(II) complexes.[22] The Aq–NH^{-} lengths in **1** and **2**·5/4 toluene, 1.323(2) and 1.328(3) Å respectively, are relatively shorter than those observed in *o*-amidophenolato(2−) complexes of transition metal ions.[23] It is analyzed as the effect of the delocalization of the negative charge over the anthraquinone fragments as illustrated in Scheme 2. It is notable that the C–C lengths of the amidophenyl ring of **1** and **2**·5/4 toluene exhibit a quinoidal distortion. The C3–C4 and C5–C6 lengths are significantly shorter, while the adjacent C–C lengths are relatively longer (Table 1). Two C=O lengths of the anthraquinone fragment differ significantly; the average C14–O16 (coordinated) lengths are 1.280(3) Å, while the average C7–O17 lengths are 1.231(3) Å.

3 crystallizes in the $P2_1/c$ space group. The bond parameters of the coordination sphere of this ruthenium(III) analogue are somewhat different from those of **1**. In **3**, the Ru^{III}–NH_{Aq}^{-}, Ru^{III}–O and Ru^{III}–Cl lengths are expectedly shorter, while the Ru^{III}–PPh_3 lengths are relatively longer as listed in Table 1. However, the bond parameters of the $AqNH^{-}$ in **1** and **3** are similar, and the Aq–NH^{-} length in **3** is 1.329(3) Å. The bond parameters of the coordination sphere and the $AqNH^{\bullet}$ ligand of the oxidized analogue attribute a different feature from that of **1**, **2**·5/4 toluene and **3**. The X-ray structure of $2^{+}I_5^{-}\cdot\frac{1}{2}I_2$ was determined at 135 and 295 K. $2^{+}I_5^{-}\cdot\frac{1}{2}I_2$ crystallizes in the $P\bar{1}$ space group. The molecular geometry of the crystals and the atom labeling schemes are shown in Fig. 2(a) and the selected bond parameters are summarized in Table 1. The X-ray bond parameters of ion 2^{+} at 135 and 295 K are approximately similar. This is the first report of the single crystal X-ray structure of an arylamino radical coordinated to a heavier transition metal ion. One of the significant features is that the $Os^{II}-NH_{Aq}^{\bullet}$ length of $2^{+}I_5^{-}\cdot\frac{1}{2}I_2$ is relatively shorter than the M^{II}–NH_{Aq}^{-} lengths of **1** and **2**·5/4 toluene. The $Os^{II}-NH_{Aq}^{\bullet}$ length is 1.978(5) Å in $2^{+}I_5^{-}\cdot\frac{1}{2}I_2$, while the Os^{II}–NH_{Aq}^{-} length in **2**·5/4 toluene is 2.037(2) Å. This reveals that the conversion of $AqNH^{-}$ to $AqNH^{\bullet}$ leads to an decrease of the M–N bond order, predicting the formation of a 2c–3e bond between a filled d-orbital and a singly occupied p-orbital of the nitrogen atom.

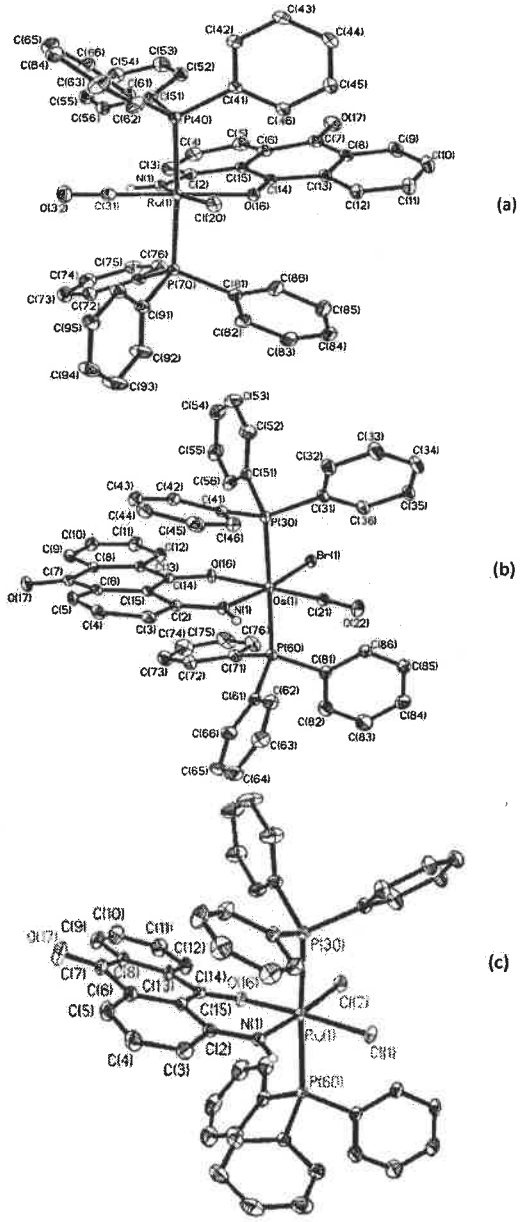

Fig. 1 Molecular geometries of (a) **1**, (b) **2**·5/4 toluene and (c) **3** with 40% thermal ellipsoids (H atom and toluene molecule are omitted for clarity).

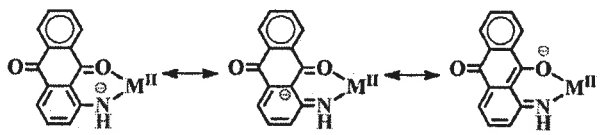

Scheme 2

The similar trend, $M-NH_{Aq}^{-} > M-NH_{Aq}^{\bullet}$, was also documented in the X-ray structures of the anilinyl radical complexes of nickel(II) and cobalt(II) ions.[7] Due to the coordination of the

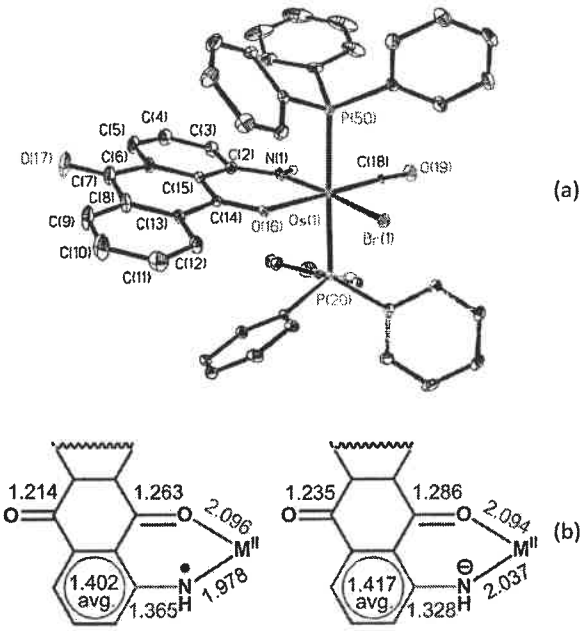

Fig. 2 (a) Molecular geometry of $2^+I_5^-\cdot\frac{1}{2}I_2$ in crystals (40% thermal ellipsoids, H atom, I_2 and I_5^- are omitted for clarity) and (b) selected bond lengths (Å) of [Os^{II}(AqNH$^-$)] and [Os^{II}(AqNH$^\cdot$)] fragments.

anionic AqNH$^-$, $d_\pi \rightarrow$ CO and $d_\pi \rightarrow PPh_3$ back bonding in **1** and **2** are relatively stronger, while because of the AqNH$^\cdot$ coordination, the cation is a 17e species and the effect of back bonding is less in ion 2^+, resulting in the relatively longer M^{II}–CO and M^{II}–PPh_3 lengths.

In the cation, the Os^{II}–CO length is 1.915(6) Å and the average Os^{II}–PPh_3 lengths are 2.432(2) Å, while the Os^{II}–CO length in 2·5/4 toluene is 1.844(3) Å. However, the M^{II}–O lengths in **1**, 2·5/4 toluene and $2^+I_5^-\cdot\frac{1}{2}I_2$ are approximately similar. The Os^{II}–Br bond *trans* to the σ-donor AqNH$^-$ in 2·5/4 toluene is relatively longer than that *trans* to AqNH$^\cdot$ in $2^+I_5^-\cdot\frac{1}{2}I_2$.

In the reported anilinyl radical complexes, no significant change of the bond parameters of the AqNH$^-$ and AqNH$^\cdot$ states was recorded.[7] In comparison, the bond parameters of the AqNH$^-$ and AqNH$^\cdot$ states in 2·5/4 toluene and $2^+I_5^-\cdot\frac{1}{2}I_2$ are notably different, as shown in Fig. 2(b). The Aq–NH$^\cdot$ length, 1.365(8) Å in $2^+I_5^-\cdot\frac{1}{2}I_2$, is longer than the average Aq–NH$^-$ lengths, 1.326(2) Å in **1** and 2·5/4 toluene. In $2^+I_5^-\cdot\frac{1}{2}I_2$ the quinoidal distortion of the aminophenyl ring is relatively less than that of the amidophenyl rings in **1** and 2·5/4 toluene, as listed in Table 1. It is noteworthy that the average C–C lengths of the amidophenyl ring of **1** and 2·5/4 toluene are 1.415(4) and 1.417(4) Å, while the average C–C lengths of the aminophenyl ring of $2^+I_5^-\cdot\frac{1}{2}I_2$ are relatively shorter, 1.402(10) Å, and correspond to those of an aromatic ring. The bond lengths of the anthraquinone fragment are less perturbed in $2^+I_5^-\cdot\frac{1}{2}I_2$. The coordinated C=O lengths of $2^+I_5^-\cdot\frac{1}{2}I_2$, 1.263(7) Å, are relatively shorter than those in **1** and 2·5/4 toluene.

Redox activities

The redox activities of the complexes were investigated by cyclic voltammetry in CH_2Cl_2 at 295 K. The cyclic voltammograms are illustrated in Fig. 3 and the redox potential data referenced to the Fc^+/Fc couple are summarized in Table 2. **1** exhibits two anodic redox waves at +0.14 and +1.02 V. Estimating the ratio of the peak currents (forward, $i_{p,f}$ and return, $i_{p,r}$), the former is reversible ($i_{p,f}/i_{p,r}$ = 1.01) and is assigned to the AqNH$^\cdot$/AqNH$^-$ redox couple. The cyclic voltammogram of **2** is similar to that of **1** and both anodic waves of **2** at +0.05 ($i_{p,f}/i_{p,r}$ = 1.01) and +0.84 V ($i_{p,f}/i_{p,r}$ = 1.0) due to the AqNH$^\cdot$/AqNH$^-$ and Os^{III}/Os^{II} redox couples being reversible. The AqNH$^\cdot$/AqNH$^-$ redox couple of **3** appears at +0.35 V. The redox potential data predict that the AqNH$^-$ of **2** is easier to oxidize than that of **1** and **3**, and the 2^+ ion was successfully isolated chemically. In solution the 2^+ ion is stable and it exhibits similar redox waves as of **2**, as shown in Fig. 3(d).

The I_2/I^- redox wave of $2^+I_5^-\cdot\frac{1}{2}I_2$ is observed at −0.33 V. The cathodic waves of **1** and **2** at −1.60 ($i_{p,f}/i_{p,r}$ = 1.04) and −1.48 V ($i_{p,f}/i_{p,r}$ = 1.01) are reversible and assigned to the AqNH$^-$/

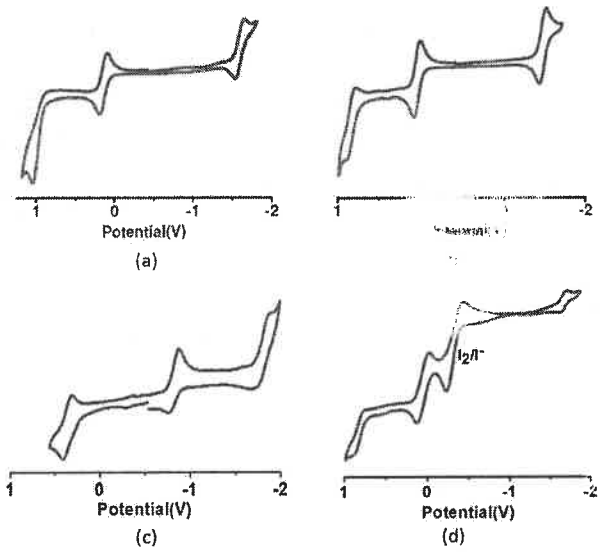

Fig. 3 Cyclic voltammograms of (a) **1**, (b) **2**, (c) **3** and (d) $2^+I_5^-\cdot\frac{1}{2}I_2$ in CH_2Cl_2 at 295 K. Conditions: scan rate, 100 mV s^{-1}; 0.20 M [N(*n*-Bu)$_4$]PF_6 supporting electrolyte; platinum working electrode.

Table 2 Redox potentials of **1**–**3** and $2^+I_5^-\cdot\frac{1}{2}I_2$ determined by cyclic voltammetry in CH_2Cl_2 (0.20 M [N(*n*-Bu)$_4$]PF_6 supporting electrolyte at 295 K)

Complexes	M^{III}/M^{II}, V (ΔE,[a] mV)	AqNH$^\cdot$/AqNH$^-$, V (ΔE,[a] mV)	$Aq_1^{NH}SQ^{\cdot 2-}$, V (ΔE,[a] mV)
1	+1.02[b]	+0.14 (105)	−1.60 (110)
2	+0.84 (95)	+0.05 (80)	−1.48 (80)
3	−1.76 (180)	+0.35 (100)	−0.86 (115)
2^+	+0.83 (115)	+0.06(120)	−1.66 (70), −0.33 (210)

[a] Peak-to-peak separation in mV. [b] Anodic peak potential.

$Aq^{NH}SQ^{\cdot 2-}$ redox couple, while the redox wave of **3** at −0.86 ($i_{p,f}/i_{p,r}$ = 1.60) V is not quite reversible. The cathodic wave of **3** at −1.76 V due to the Ru^{III}/Ru^{II} redox couple is irreversible.

EPR spectroscopy

The measurement of magnetic susceptibility authenticated that $2^+I_5^-\cdot\frac{1}{2}I_2$ and **3** are one electron paramagnetic. The variable temperature EPR spectra of the 1^+, 2^+, 1^- and 2^- ions in CH_2Cl_2 and the frozen CH_2Cl_2 glass EPR spectrum of **3** were recorded and the spectral parameters are listed in Table 3. The CH_2Cl_2 frozen glass EPR spectrum of **3** is depicted in Fig. 4(a). The *g*-values are g_1 = 2.386, g_2 = 2.075 and g_3 = 1.820, which correspond to those of the ruthenium(III) complexes[24] with larger *g* anisotropy (Δg = 0.56). The shape of the EPR spectrum of **3** is different from that of a typical rhombic spectrum of an octahedral ruthenium(III) ion. However, such spectra are documented in the literature in many instances.[6,24]

Table 3 X-band EPR spectral parameters of **3**, 1^+, $2^+I_5^-\cdot\frac{1}{2}I_2$, 1^- and 2^- in CH_2Cl_2

	Conditions	*g*-Values
3	Frozen glass at 115 K	2.386, 2.075, 1.820
1^+	Solution at 295 K	2.014 A_P = 33 (^{31}P, $I=\frac{1}{2}$), A_H = 13 (^{1}H, $I=\frac{1}{2}$) A_N = 10 (^{14}N, I = 1), A_{Cl} = 4.8 G (^{35}Cl, I = 3/2)
1^+	Frozen glass at 115 K	
	$[(AqNH^{\cdot})Ru^{II}]$ component	2.004
	$[(AqNH^{-})Ru^{III}]$ component	2.000, 2.002, 2.060
2^+	Solution at 295 K	2.027
2^+	Frozen glass at 115 K	
	$[(AqNH^{\cdot})Os^{II}]$ component	1.998
	$[(AqNH^{-})Os^{III}]$ component	1.933, 1.992, 2.165
2^+	Powder at 295 K	
	$[(AqNH^{\cdot})Os^{II}]$ component	1.994
	$[(AqNH^{-})Os^{III}]$ component	2.040
2^+	Powder at 115 K	
	$[(AqNH^{\cdot})Os^{II}]$ component	1.994
	$[(AqNH^{-})Os^{III}]$ component	1.940, 1.994, 2.170
1^-	Solution at 295 K	2.005
1^-	Frozen glass at 115 K	2.005
2^-	Solution at 295 K	2.006, 2.011
2^-	Frozen glass at 115 K	
	$[(Aq^{NH}SQ^{\cdot 2-})Os^{II}]$ component	2.003
	$[(Aq^{NH}SQ^{3-})Os^{III}]$ component	1.999, 2.000, 2.025

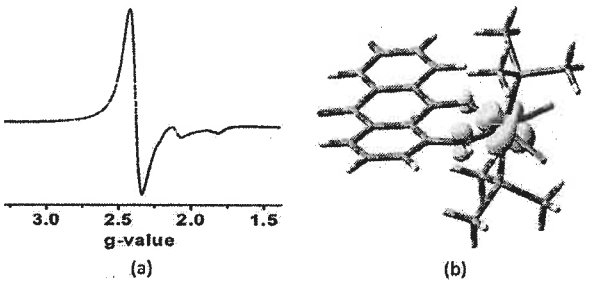

Fig. 4 (a) X-band EPR spectrum of the frozen CH_2Cl_2 glass of **3** and (b) atomic spin of 3^{Me} (Ru, 0.84) obtained from Mulliken spin population analysis.

The 3^+ ion contains an $AqNH^{\cdot}$ radical that results in antiferromagnetic coupling with the paramagnetic ruthenium(III) ion, and is EPR silent. The EPR spectra of the 1^+ and 2^+ ions are significantly different from that of **3**. The variable temperature (295–115 K) X-band EPR spectra of the electro-generated 1^+ ion in CH_2Cl_2 are depicted in Fig. 5(a). The *g*-parameters obtained from the simulation are summarized in Table 3. The EPR spectrum of the 1^+ ion in CH_2Cl_2 at 295 K exhibits hyperfine couplings due to ^{31}P, (A_P = 33 G, $I=\frac{1}{2}$), ^{1}H (A_H = 13 G, $I=\frac{1}{2}$), ^{14}N (A_N = 10 G, I = 1) and ^{35}Cl (A_{Cl} = 4.8 G, I = 3/2) nuclei as shown in Fig. 5(b), and the simulated *g* value is 2.014, which corresponds well to the $[Ru^{II}(AqNH^{\cdot})]$ state. The slightly higher value of *g* than those of pure organic radicals[25] indicates a contribution of the ruthenium(III) state to the SOMO.

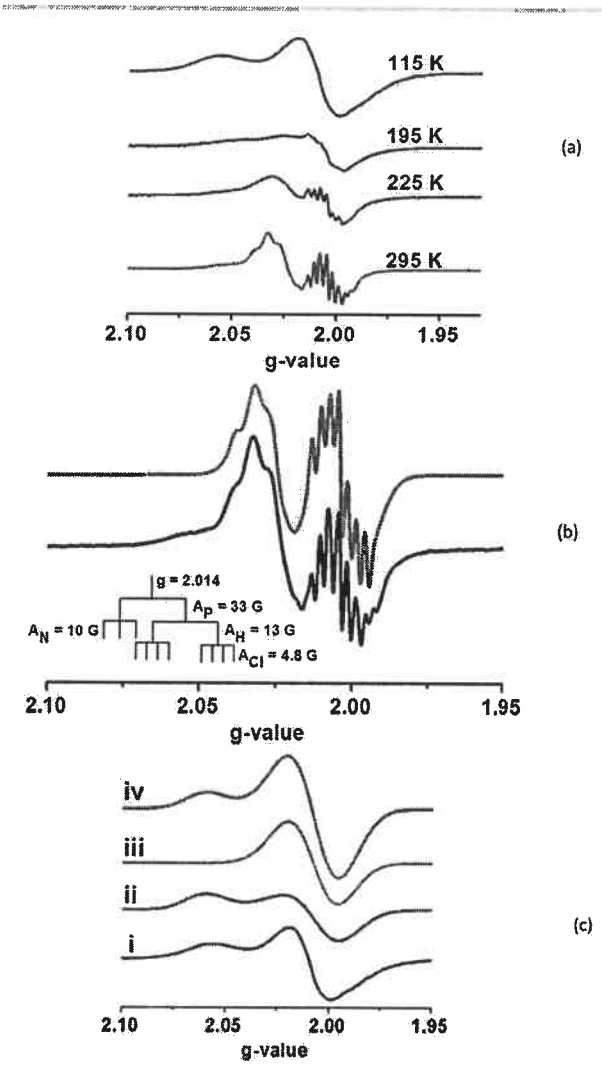

Fig. 5 (a) Variable temperature (295–115 K) X-band EPR spectra of 1^+, (b) simulation of the fluid solution EPR spectrum and (c) simulation of the frozen CH_2Cl_2 glass EPR spectrum (black (i), experimental; blue (ii), simulated spectrum considering the $[Ru^{III}(AqNH^{-})]$ state; green (iii), simulated spectrum considering the $[Ru^{II}(AqNH^{\cdot})]$ state; red (iv), simulated spectrum considering both the $[Ru^{III}(AqNH^{-})]$ and $[Ru^{II}(AqNH^{\cdot})]$ (1 : 1) components).

Thus, in fluid solution the 1^+ ion is an AqNH$^\bullet$ complex of ruthenium(II). The CH_2Cl_2 frozen glass EPR spectrum of the 1^+ ion is somewhat different. The spectrum was simulated considering the contributions of the $[Ru^{II}(AqNH^\bullet)]$ and $[Ru^{III}(AqNH^-)]$ resonance states as depicted in Fig. 5(c). The simulated spectrum iii of Fig. 5(c) with $g = 2.004$ corresponds to the $[Ru^{II}(AqNH^\bullet)]$ state, while the rhombic signal (presented by the spectrum ii) with $g_1 = 2.000$, $g_2 = 2.002$ and $g_3 = 2.060$ ($g_{av} = 2.021$) corresponds to the $[Ru^{III}(AqNH^-)]$ state.

The variable temperature EPR spectra of $2^+I_5^-\cdot\frac{1}{2}I_2$ in CH_2Cl_2 are illustrated in Fig. 6(a). The isotropic EPR signal of $2^+I_5^-\cdot\frac{1}{2}I_2$ in CH_2Cl_2 is relatively broader as illustrated in Fig. 6(b), and hyperfine splitting is not observable. The simulated g value, 2.027, deviates significantly[7b] from those recorded for organic radicals, predicting a larger contribution of the osmium(III) state to the SOMO. The frozen glass EPR spectrum of the 2^+ ion at 115 K was successfully simulated considering the $[Os^{II}(AqNH^\bullet)]$ and $[Os^{III}(AqNH^-)]$ states as shown in Fig. 6(c). The spectrum is composed of an isotropic signal at $g = 1.998$ due to the $[Os^{II}(AqNH^\bullet)]$ state (motif **A** of Scheme 3) and an anisotropic rhombic signal with $g_1 = 1.933$, $g_2 = 1.992$ and $g_3 = 2.165$ due to the $[Os^{III}(AqNH^-)]$ state, defined by motif **B**. The anisotropy of the rhombic component of the frozen glass EPR spectrum of the 2^+ ion is relatively larger than that of the 1^+ ion, inferring a larger contribution of the $[M^{III}(AqNH^-)]$ state to the 2^+ ion.

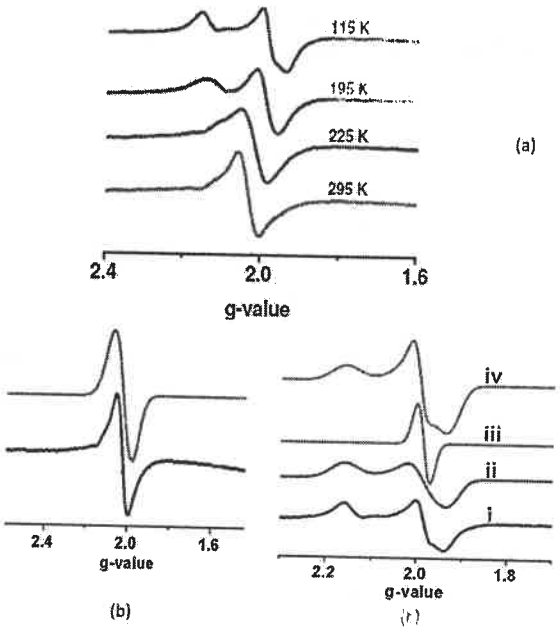

Fig. 6 (a) Variable temperature (295–115 K) X-band EPR spectra of $2^+I_5^-\cdot\frac{1}{2}I_2$ in CH_2Cl_2; (b) simulation of the fluid solution EPR spectrum and (c) simulation of the frozen CH_2Cl_2 glass EPR spectrum (black (i), experimental; blue (ii) simulated spectrum considering the $[Os^{III}(AqNH^-)]$ state; green (iii), simulated spectrum considering the $[Os^{II}(AqNH^\bullet)]$ state; red (iv) simulated spectrum considering both the $[Os^{III}(AqNH^-)]$ and $[Os^{II}(AqNH^\bullet)]$ (1 : 1) components).

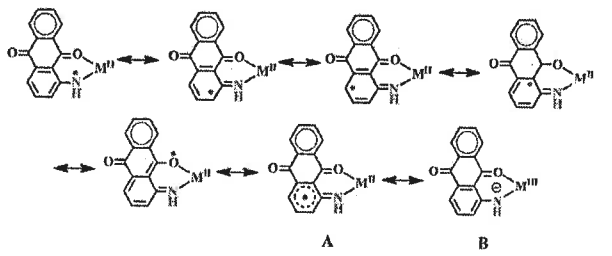

Scheme 3

The EPR spectroscopy of the powder sample also authenticated the contribution of states **A** and **B** [illegible]. The EPR signal at 295 K is relatively broader. It was considered considering the contributions of the $[Os^{II}(Aq$ [illegible] $[Os^{III}(AqNH^-)]$ states as shown in Fig. 7(a), where the simulated spectrum ii corresponds to the $[Os^{III}(AqNH^-)]$ state and the spectrum iii is for the $[Os^{II}(AqNH^\bullet)]$ state. In the frozen glass at 115 K the spectrum ii resolves well to a rhombic spectrum, with $g_1 = 1.940$, $g_2 = 1.994$ and $g_3 = 2.170$ as depicted in Fig. 7(b). The study infers the delocalization of the spin of these 17e species over the metal and ligand fragment, and having a hybrid of the $[M^{II}(AqNH^\bullet)]$ and $[M^{III}(AqNH^-)]$ states as the ground electronic state.

The EPR spectra of the 1^- and 2^- ions obtained after reduction of **1** and **2** by cobaltocene in CH_2Cl_2 were recorded at 295 K and 115 K. The variable temperature spectra of the 1^- ion are depicted in Fig. 8(a). It is notable that the isotropic signal of 1^- in CH_2Cl_2 remains unperturbed even in the frozen glass and the experimental g value is 2.005 [illegible] corroborates well to those reported in cases of 9,10-anthraquinonate anion radicals.[26] Thus, the ground electronic state of 1^- is consistent with the $[Ru^{II}(Aq^{NH}SQ^{\bullet-2-})]$ description. Unfortunately, the hyperfine splitting due to aromatic nitrogen atoms is not observable in this coordination complex.

The fluid solution and frozen glass EPR spectra of 2^- are different from those of the 1^- ion. In the frozen glass spectrum the contribution of an anisotropic component to the 2^- ion is

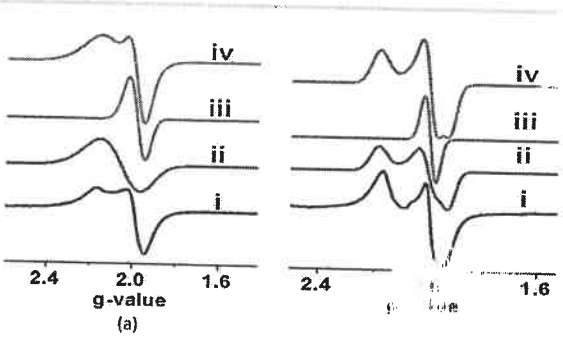

Fig. 7 X-band EPR spectra of the powder [illegible] (a) 295 K and (b) 115 K (black (i), experimental; blue (ii) simulated spectrum considering the $[Os^{III}(AqNH^-)]$ state; green (iii), simulated spectrum considering the $[Os^{II}(AqNH^\bullet)]$ state; red (iv) simulated spectrum considering both the $[Os^{III}(AqNH^-)]$ and $[Os^{II}(AqNH^\bullet)]$ (1 : 1) resonance states).

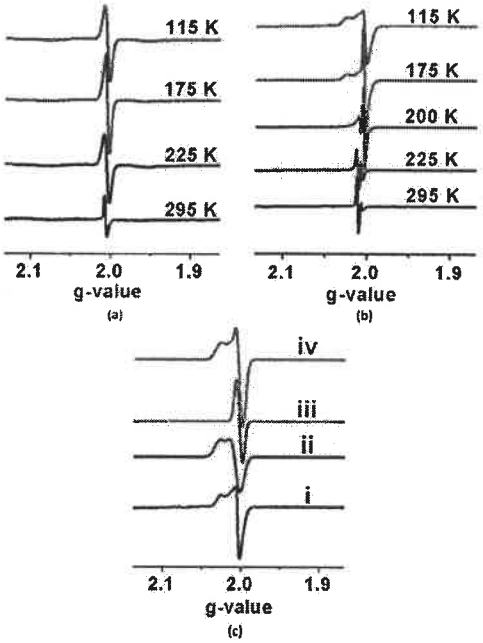

Fig. 8 Variable temperature (295–115 K) X-band EPR spectra of (a) 1^-, (b) 2^- in CH_2Cl_2 and (c) simulation of the frozen CH_2Cl_2 glass EPR spectrum of 2^- (black (i), experimental; blue (ii) simulated spectrum considering the $[Os^{III}(Aq^{NH}SQ^{3-})]$ state; green (iii), simulated spectrum considering the $[Os^{II}(Aq^{NH}SQ^{\cdot 2-})]$ state; red (iv) simulated spectrum considering both the $[Os^{III}(Aq^{NH}SQ^{3-})]$ and $[Os^{II}(Aq^{NH}SQ^{\cdot 2-})]$ (1 : 1) resonance states).

detected. At 295 K, the g value of the major signal of the 2^- ion is 2.011, while the g value of the major signal at 175 K is 2.006. Comparing the fluid solution EPR spectrum of the 2^+ ion, which exhibits a signal at 2.027 as reported above, the EPR signal of the 2^- ion at g = 2.011 is assigned to state **E** of Scheme 4. The EPR signal of the 2^- ion at g = 2.006 is consistent with the $[Os^{II}(Aq^{NH}SQ^{\cdot 2-})]$, **C** state, while the frozen glass EPR spectrum was simulated considering isotropic and anisotropic components due to the $[Os^{II}(Aq^{NH}SQ^{\cdot 2-})]$, **C**, and $[Os^{III}(Aq^{NH}SQ^{3-})]$, **D**, states as described in the caption of Fig. 8(c). The study reveals that similar to the 2^+ ion, the contribution of the M(III) state to the 2^- ion is significant.

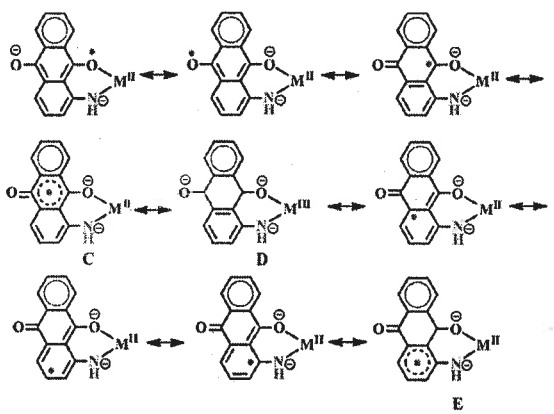

Scheme 4

DFT calculations

DFT calculations of the complexes at the B3LYP level of theory were employed to elucidate the electronic structures of the 1^+, 2^+, 1^-, 2^- and 3^+ ions. Gas phase geometries of the PMe_3 analogues of the $AqNH^-$ complexes, *trans*-$[Ru^{II}(AqNH^-)(PMe_3)_2(CO)Cl]$ (1^{Me}), *trans*-$[Os^{II}(AqNH^-)(PMe_3)_2(CO)Br]$ (2^{Me}) and *trans*-$[Ru^{III}(AqNH^{\cdot})(PMe_3)_2Cl_2]^+$ (3^{Me+}) were optimized with the singlet spin state, while the $AqNH^{\cdot}$ analogues, 1^{Me+}, 2^{Me+}, 1^{Me-}, 2^{Me-} and 3^{Me} ions were optimized with the doublet spin state using LANL2DZ basis sets for the metal ions. Based on these coordinates, the ground state energies of the 1^{Me+}, 2^{Me+}, 1^{Me-} and 2^{Me-} ions were calculated in CH_2Cl_2 using the CPCM model. The ground state energies of the **1**, **2** and 2^+ ions in CH_2Cl_2 were also calculated using the crystallographic coordinates. The optimized coordinates are listed in Table S4–S14.† The calculated bond parameters of 1^{Me}, 2^{Me}, 2^{Me+} and 3^{Me} correlate well to those obtained from the single crystal structure determinations of **1**, 2·5/4 toluene, $2^+I_5^-\cdot\frac{1}{2}I_2$ and **3** as summarized in Table 1. The calculated bond parameters of the 1^{Me}, 2^{Me}, 3^{Me}, 1^{Me+}, 2^{Me+}, 3^{Me+}, 1^{Me-} and 2^{Me-} ions are listed in Table S2.† As observed experimentally, the calculated M–O, $M–NH_{Aq}^-$ and M–X lengths are longer in 1^{Me} and 2^{Me} than those in the 1^{Me+} and 2^{Me+} ions, while the M–CO and $M–PPh_3$ lengths are relatively shorter in 1^{Me} and 2^{Me}. The calculated $M^{II}–NH_{Aq}^-$ lengths are relatively longer than those of $M^{II}–NH_{Aq}^{\cdot}$ and the trend is consistent with that established by X-ray diffraction studies. The $Ru^{II}–NH_{Aq}^-$ length in 1^{Me} is 2.073 Å, while the $Ru^{II}–NH_{Aq}^{\cdot}$ length in 1^{Me+} is 1.989 Å. Similarly, the calculated $Os^{II}–NH_{Aq}^-$ and $Os^{II}–NH_{Aq}^{\cdot}$ lengths in 2^{Me} and 2^{Me+} are 2.065 and 1.992 Å respectively, while the corresponding experimental lengths are, 2.017(11) and 1.978(5) Å respectively. A molecular orbital analysis affirmed that in the cations a singly occupied nitrogen p-orbital of $AqNH^{\cdot}$ promotes a π-bonding interaction (2c–3e type) with a d-orbital of the metal increasing the $M–NH_{Aq}^{\cdot}$ bond multiplicity. The occupied orbitals (β-HOMO and β-HOMO–1) are shown in Fig. 9(a) and (b). The corresponding antibonding π^*_{Os-N} orbitals are a singly occupied α-SOMO and an unoccupied β-LUMO as illustrated in Fig. 9.

The calculated C=O lengths (coordinated to the metal ion) of the anthraquinone fragment in 1^{Me} and 2^{Me} are 1.270 and 1.277 Å respectively, while these are relatively shorter in 1^{Me+} and 2^{Me+} (1.258 and 1.265 Å respectively). On the contrary, the corresponding C=O lengths are relatively longer in the 1^{Me-} (1.304 Å) and 2^{Me-} (1.309 Å) ions. The M–O, M–CO and $M–PPh_3$ lengths of the 1^{Me-} and 2^{Me-} ions are shorter than those in 1^{Me} and 2^{Me}. The features predict that the 19e anionic species promote stronger back bonding than the 18e neutral and 17e cationic species.

The atomic spin of the 1^{Me+}, 2^{Me+}, 1^{Me-} and 2^{Me-} ions obtained from Mulliken spin population analyses are illustrated in Fig. 10. In the cations, the spin scatters on the nitrogen and metal atoms. However, the percentage of the spin on

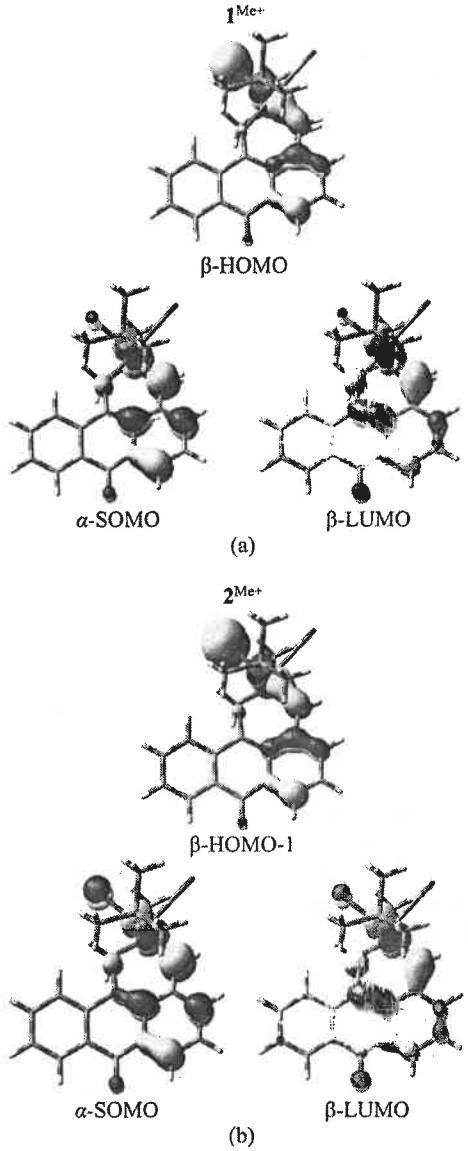

Fig. 9 2c–3e p_π–d_π bonding interactions and related occupied bonding, singly occupied and unoccupied antibonding orbitals of (a) 1^{Me+} and (b) 2^{Me+}.

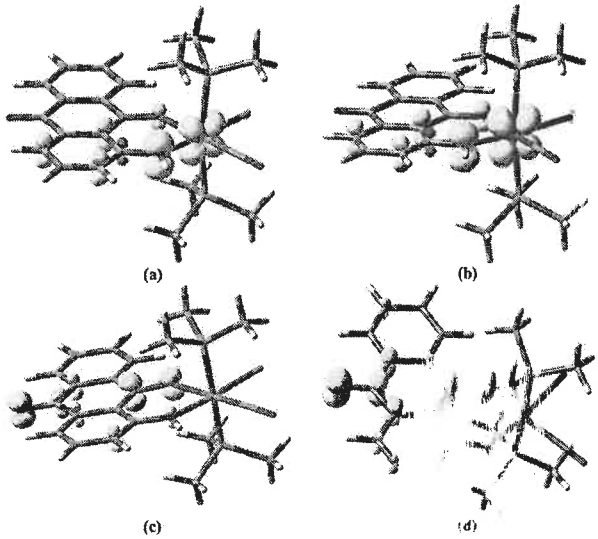

Fig. 10 Atomic spin of (a) 1^{Me+} (N1, 0.35; Ru, 0.44); (b) 2^{Me+} (N1, 0.27; Os, 0.56); (c) 1^{Me-} (N1, 0.04; C3, 0.11; C5, 0.06; C7, 0.06; C14, 0.20; O16, 0.12; O17, 0.19) and (d) 2^{Me-} (N1, 0.05; C3, 0.10; C5, 0.07; C7, 0.06; C14, 0.21; O16, 0.11; O17, 0.19) ions obtained from Mulliken spin population analyses.

the nitrogen and metal atoms differs in the gas phase and in solution. It is notable that in the 1^{Me+} ion (in CH_2Cl_2 using the CPCM model) 56% of the atomic spin is localized on the ligand backbone, with 35% spin in one of the p-orbitals of the nitrogen atom. The rest of the spin disperses on the aromatic ring and the coordinated oxygen atom, predicting an $AqO^{\bullet}$ state of the $AqNH^{\bullet}$ radical as shown in Scheme 3. The atomic spin in the 2^{Me+} ion depicts a similar pattern with 44% on the ligand (27% being at the nitrogen atom) and 56% on the osmium ion. The atomic spin distribution of the 2^+ ion in CH_2Cl_2 obtained from the X-ray coordinates of $2^+I_5^-\cdot\frac{1}{2}I_2$ follows a similar trend ($AqNH^{\bullet}$, 45%). The sharing of the spin by the nitrogen and metal atoms supports the formation of M–N bonds. On the contrary, in the 1^{Me-} and 2^{Me-} ions the spin is primarily localized on the quinone fragment as depicted in Fig. 10(c) and (d), and the anions are defined by 9,10-anthrasemiquinonate anion radical states of types $[Ru^{II}(Aq^{NH}SQ^{\bullet 2-})]$ and $[Os^{II}(Aq^{NH}SQ^{\bullet 2-})]$. The trend of the calculated coupling constants, A_P = 17 (^{31}P, $I = \frac{1}{2}$), A_H = 8.6 (^1H, $I = \frac{1}{2}$), A_N = 7.4 (^{14}N, I = 1) and A_{Cl} = 0.8 G (^{35}Cl, I = 3/2), is similar to that of the 1^+ ion observed experimentally (Table 3). For the 2^+ ion, the coupling constants are smaller (5.5, 3.4, and 0.7 G due to the ^{14}N, ^{79}Br, ^{15}P and ^1H nuclei), while the spin is negligible for the 1^{Me-} and 2^{Me-} ions, correlating the observations that the 2^+, 1^- and 2^- ions do not exhibit hyperfine EPR spectra. The calculated coupling constants of 1^{Me-} due to ^{14}N, ^{35}Cl, ^{15}P and seven ^1H nuclei of the anthraquinone fragment are 1.23, 0.07, 0.74 and 0.16–2.34 G.

The Mulliken spin obtained from unrestricted B3LYP calculations on 3^{Me} is dominantly localized on the ruthenium as depicted in Fig. 4(b), authenticating that 3 is a ruthenium(III) complex. The closed shell singlet (CSS) solution of 3^{Me+} is stable, and no perturbation due to the open shell singlet (OSS) state is observed. However, the energy of the triplet solution of 3^{Me+} is only 3.5 kJ mol^{-1} higher than that of the CSS solution, inferring a significant contribution of the coupled di-radical state, '$[Ru^{III}(AqNH^{\bullet})]$', to the ground electronic state of 3^+. The calculated M–NH_{Aq} and Aq–NH lengths of 3^{Me+} are significantly different from those in 3^{Me}. The calculated Ru^{III}–$NH^{\bullet}_{Aq}$ length, 1.899 Å, in 3^{Me+} is relatively shorter than the Ru^{III}–NH_{Aq}^- length, 1.994 Å, in 3^{Me}, while the Aq–NH length, 1.377 Å, in 3^{Me+} is longer than the Aq–$NH^{\bullet -}$ length, 1.341 Å, in 3^{Me}. The trend is similar to that observed in the $1 \rightarrow 1^+$ and $2 \rightarrow 2^+$ conversions.

Electronic spectra

The UV-vis-NIR absorption spectra of **1–3** were recorded in CH_2Cl_2 at 295 K. The spectra are illustrated in Fig. 11 and the absorption data are listed in Table 4. The UV-vis-NIR absorption spectra of the cations were recorded by spectroelectrochemical measurements during the conversions of **1**→**1**$^+$, **2**→**2**$^+$ and **3**→**3**$^+$ in CH_2Cl_2 (Fig. 12(a)–(c)). The general observation is that the lower energy absorption bands of **1**, **2** and **3** are blue shifted in the **1**$^+$, **2**$^+$ and **3**$^+$ ions. The spectrum of **1** displays a lower energy absorption maximum at 725 nm with shoulders at 800 and 660 nm, while the absorption band of the **1**$^+$ ion is relatively broader and hypsochromically shifted to 500–700 nm. The absorption maximum of **1**$^+$ at 450–650 nm is absent in **1**. **2** exhibits an absorption band maximum at 760 nm with shoulders at 840 and 685 nm, however the absorption band of **2**$^+$ is relatively broader and blue shifted to 660–850 nm. Similarly, the absorption peak of **3** at 530 nm hypsochromically shifted to 455 nm in the **3**$^+$ ion.

The origins of the lower energy absorption bands of the diamagnetic complexes were elucidated by the time dependent (TD) DFT calculations on AqNH$^-$, **1**^{Me} and **2**^{Me} in CH_2Cl_2 using the CPCM model. It is established that the –NH$^-$ function is a charge donor. It is calculated that AqNH$^-$ absorbs at 699.37 nm due to the intra-ligand $p_N \rightarrow \pi^*_{Ar}$ (f = 0.12) charge transfer. For **1**^{Me} the calculated excitation at 732.22 nm is due to the $p_N + d_{Ru} \rightarrow \pi^*_{Ar}$ (f = 0.07) transition. The similar transition in **2**^{Me} appears at 804.52 nm as summarized in Table S3.† The related photoactive orbitals of AqNH$^-$, **1**^{Me} and **2**^{Me} are depicted in Fig. S2.† The hypsochromic shift of the absorption band of **1**$^+$ to 500–700 nm is due to the oxidation of AqNH$^-$ to AqNH$^\bullet$. Similar features of the absorptions was recorded during the **2**→**2**$^+$ conversion, due to the formation of AqNH$^\bullet$. The characteristic absorption bands of the cations are absent in the reduced anions. However, during the **1**→**1**$^-$, **2**→**2**$^-$ and **3**→**3**$^-$ conversions the intensities of the lower energy absorption bands of **1–3** decrease as illustrated in Fig. 12(d)–(f), which may be due to reduction of the acceptor quinone to the semiquinonate state.

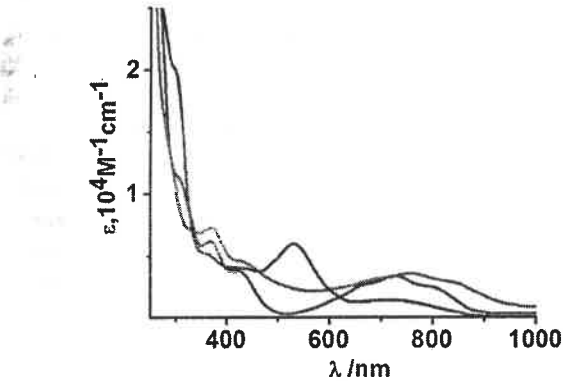

Fig. 11 UV-vis-NIR absorption spectra of **1** (violet), **2** (red) and **3** (blue) in CH_2Cl_2 at 295 K.

Table 4 UV-vis-NIR spectral data of **1–3**, [**1–3**]$^+$, [**1–3**]$^-$ and **2**$^+$$I_5^-$·$\frac{1}{2}I_2$ in CH_2Cl_2 at 295 K

Complexes	λ_{max} (nm) (ε, 10^4 M^{-1} cm^{-1})
1	800 (0.25), 725 (0.35), 660 (0.3), 421 (0.4), 365 (0.6)
1$^+$	930 (0.04), 800 (0.15), 720 (0.24), 555 (0.23), 425 (0.32), 365 (0.52)
1$^-$	805 (0.11), 720 (0.16), 655 (0.15), 440 (0.40), 370 (0.67)
2	840 (0.30), 760 (0.36), 685 (0.3), 430 (0.45), 370 (0.73)
2$^+$	1000 (0.14), 845 (0.32), 770 (0.34), 670 (0.39), 415 (0.8), 380 (0.92), 360 (0.90)
2$^+$$I_5^-$·$\frac{1}{2}I_2$	840 (0.24), 760 (0.31), 675 (0.24), 485 (0.40), 365 (1.12), 280 (1.98)
2$^-$	1000 (0.11), 840 (0.30), 770 (0.34), 675 (0.33), 425 (0.73), 370 (0.96)
3	720 (0.20), 530 (0.60), 430 (0.45), 360 (0.55)
3$^+$	720 (0.16), 455 (0.54), 355 (0.60)
3$^-$	660 (0.27), 530 (0.44), 440 (0.43)

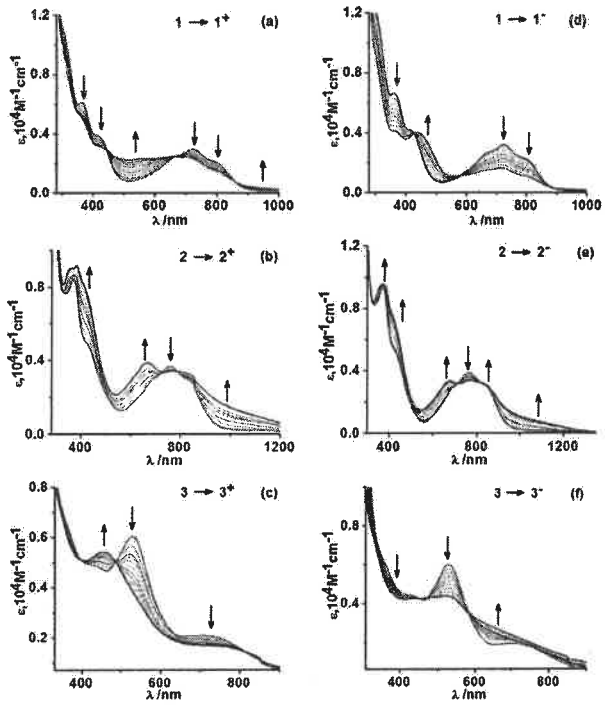

Fig. 12 Spectroelectrochemical measurements showing the change of the electronic spectra during the conversions of (a) [**1**→**1**$^+$], (b) [**2**→**2**$^+$], (c) [**3**→**3**$^+$], (d) [**1**→**1**$^-$], (e) [**2**→**2**$^-$] and (f) [**3**→**3**$^-$] in CH_2Cl_2 at 295 K.

Conclusions

The article reports on a family of 1-amido-9,10-anthraquinone (AqNH$^-$) and 1-amino-9,10-anthraquinone radical (AqNH$^\bullet$) complexes of ruthenium(II/III) and osmium(II) ions. The nitrogen centred radicals like ArNH$^\bullet$ and aminyl ($R_2N^\bullet$) are less stable, but from a fundamental and biological perspective, isolation of these radicals is worthy. In this work, AqNH$^-$ and AqNH$^\bullet$ complexes were successfully isolated and characterized by X-ray crystallography, setting the example of the first X-ray

structure of an arylamino radical with a heavier transition metal ion. Moreover, 1-amido-9,10-anthrasemiquinonate anion radicals ($Aq^{NH}SQ^{\bullet 2-}$) coordinated to ruthenium(II/III) and osmium(II) ions were conveniently generated. Both $AqNH^{\bullet}$ and $Aq^{NH}SQ^{\bullet 2-}$ radical states were derived from 1-amino-9,10-anthraquinone ($AqNH_2$), which is defined as a molecule of dual radical counter. The study discloses the subtle differences of the metrical parameters of the $[M^{II}(AqNH^{-})]$ and $[M^{II}(AqNH^{\bullet})]$ states; $M^{II} - NH^{\bullet}_{Aq} < M^{II} - NH_{Aq}^{-}$, while $Aq\text{–}NH^{\bullet} > Aq\text{–}NH^{-}$ lengths. It is analyzed that $AqNH^{\bullet}$ attributes a π-bonding interaction with a d-orbital of the metal ion leading to a 2c–3e type of bond. This increases the multiplicity of the $M^{II} - NH^{\bullet}_{Aq}$ bond, which is not observed in the case of the $AqNH^{-}$ state. Thus, the $M^{II} - NH^{\bullet}_{Aq}$ lengths are significantly shorter than the $M^{II}\text{–}NH_{Aq}^{-}$ lengths. DFT calculations predicted that the atomic spin disperses over the metal ions and the ligand backbone, particularly in the p-orbitals of the nitrogen atom of the 1^{+} and 2^{+} ions, supporting the notion of the formation of 2c–3e M–N bonds in the $AqNH^{\bullet}$ complexes. In the 1^{-} and 2^{-} ions, the spin is dominantly localized on the anthraquinone fragment. The hypsochromic shifts of the lower energy UV-vis transitions during the $1 \rightarrow 1^{+}$, $2 \rightarrow 2^{+}$ and $3 \rightarrow 3^{+}$ conversions due to the formation of $AqNH^{\bullet}$ were established by the spectroelectrochemical measurements.

Acknowledgements

S. B. (08/531(0006)/2012-EMR-I) is thankful to CSIR, New Delhi, India and S. M. is thankful to UGC, New Delhi, India (F. No. 43-214/2014(SR)) for the fellowships.

References

1 (*a*) V. J. DeRose, I. Mukerji, M. J. Latimer, V. K. Yachandra, K. Sauer and M. P. Klein, *J. Am. Chem. Soc.*, 1994, **116**, 5239–5249; (*b*) V. K. Yachandra, V. J. DeRose, M. J. Latimer, I. Mukerji, K. Sauer and M. P. Klein, *Science*, 1993, **260**, 675–679.

2 (*a*) C. T. Lyons and T. D. P. Stack, *Coord. Chem. Rev.*, 2013, **257**, 528–540; (*b*) P. Chaudhuri and K. Wieghardt, *Prog. Inorg. Chem.*, 2001, **50**, 151; (*c*) Y. Wang, J. L. DuBois, B. Hedman, K. O. Hodgson and T. D. P. Stack, *Science*, 1998, **279**, 537–540; (*d*) A. Sokolowski, J. Müller, T. Weyhermüller, R. Schnepf, P. Hildebrandt, K. Hildenbrand, E. Bothe and K. Wieghardt, *J. Am. Chem. Soc.*, 1997, **119**, 8889–8900.

3 (*a*) S. Paria, T. Ohta, Y. Morimoto, T. Ogura, H. Sugimoto, N. Fujieda, K. Goto, K. Asano, T. Suzuki and S. Itoh, *J. Am. Chem. Soc.*, 2015, **137**, 10870–10873; (*b*) A. I. O. Suarez, V. Lyaskovskyy, J. N. H. Reek, J. I. Vlugt and B. de Bruin, *Angew. Chem., Int. Ed.*, 2013, **52**, 12510–12529; (*c*) R. G. Hicks, *Angew. Chem., Int. Ed.*, 2008, **47**, 7393–7395.

4 (*a*) E. T. Hennessy and T. A. Betley, *Science*, 2013, **340**, 591; (*b*) P. R. Tentscher, S. N. Eustis, K. McNeill and J. S. Arey, *Chem. – Eur. J.*, 2013, **19**, 112[illegible] Matsumoto, H. C. Chang, M. Wazizaka, S. Ueno, A. Kobayashi, A. Nakayama, T. Taketsugu and M. Kato, *J. Am. Chem. Soc.*, 2013, **135**, 8646; (*d*) L. Ji and G. Schüürmann, *Angew. Chem., Int. Ed.*, 2012, **52**, 744; (*e*) S. Wiese, J. L. McAfee, D. R. Pahls, C. L. McMullin, T. R. Cundari and T. H. Warren, *J. Am. Chem. Soc.*, 2012, **134**, 10114; (*f*) J. A. Stubbe and W. A. van der Donk, *Chem. Rev.*, 1998, **98**, 705–762.

5 N. Penkert, T. Weyhermüller, E. Bill, P. Hildebrandt, S. Lecomte and K. Wieghardt, *J. Am. Chem. Soc.*, 2000, **122**, 9663–9673.

6 Y. Miyazato, T. Wada, J. T. Muckerman, E. Fujita and K. Tanaka, *Angew. Chem., Int. Ed.*, 2007, **46**, 5728–5730.

7 (*a*) A. Kochem, G. Gellon, O. Jarjayes, C. Philouze, N. Leconte, M. van Gastel, E. Bill and [illegible], *Chem. Commun.*, 2014, **50**, 4924–4926; (*b*) A. [illegible] Gellon, N. Leconte, B. Baptiste, C. Philouze, [illegible], M. Orio and F. Thomas, *Chem. – Eur. J.*, 20[illegible] 16721.

8 (*a*) P. Maire, M. Königsmann, [illegible]th, J. Harmer, A. Schweiger and H. Grützmacher, [illegible] *Soc.*, 2006, **128**, 6578–6580; (*b*) T. Büttner, J. Geier, G. Frison, J. Harmer, C. Calle, A. Schweiger, H. Schönberg and H. Grützmacher, *Science*, 2005, **307**, 235–238.

9 (*a*) D. Adhikari, S. Mossin, F. Basuli, J. C. Huffman, R. K. Szilagyi, K. Meyer and D. J. Mindiola, *J. Am. Chem. Soc.*, 2008, **130**, 3676; (*b*) N. P. Mankad, W. E. Antholine, R. K. Szilagyi and J. C. Peters, *J. Am. Chem. Soc.*, 2009, **131**, 3878–3880; (*c*) C.-C. Tsou, F.-T. Tsai, H.-Y. Chen, I.-J. Hsu and W.-F. Liaw, *Inorg. Chem.*, 2013, **52**, 1631–1639.

10 (*a*) M. Stylianou, C. Drouza, J. Giapintzakis, G. I. Athanasopoulos and A. D. Keramidas, *Inorg. Chem.*, 2015, **54**, 7218–7229; (*b*) J. Yuasa and S. Fukuzumi, *J. Am. Chem. Soc.*, 2007, **129**, 12912–12913; (*c*) C[illegible]nza, V. Tolis, V. Gramlich, C. Raptopoulou, A. Te[illegible] Sigalas, T. A. Kabanos and A. D. Keramidas, [illegible], 2002, 2786–2787.

11 (*a*) N. Ahmad, J. J. Levison, S. D. R[illegible] F. Uttley, *Inorg. Synth.*, 1974, **15**, 45; (*b*) [illegible]ephenson and G. J. Wilkinson, *J. Inorg. Nucl. Chem.*, [illegible], 945.

12 (*a*) G. M. Sheldrick, *ShelXS97*, Universität Göttingen, Göttingen, Germany, 1997; (*b*) G. M. Sheldrick, *ShelXL97*, Universität Göttingen, Göttingen, Germany, 1997; (*c*) G. M. Sheldrick, *XS. Version 2013/1*, Georg-August-Universität Göttingen, Göttingen, Germany, 2013; (*d*) G. M. Sheldrick, *Acta Crystallogr., Sect. A: Fundam. Crystallogr.*, 2015, **71**, 3–8; (*e*) G. M. Sheldrick, *Acta Crystallogr., Sect. C: Cryst. Struct. Commun.*, 2015, **71**, 3–8.

13 M. J. Frisch, G. W. Trucks, H. B. Schlegel, G. E. Scuseria, M. A. Robb, J. R. Cheeseman Jr., J. A. Montgomery, T. Vreven, K. N. Kudin, J. C. Burant, J. M. Millam, S. S. Iyengar, J. Tomasi, V. Barone, B. Mennucci, M. Cossi, G. Scalmani, N. Rega, G. A. Peters[illegible] Nakatsuji, M. Hada, M. Ehara, K. Toyota, R. F[illegible] Hasegawa, M. Ishida, T. Nakajima, Y. Honda, [illegible] Nakai, M. Klene, X. Li, J. E. Knox, H. P. H[illegible] B. Cross, V. Bakken, C. Adamo, J. Ja[illegible] Gomperts,

R. E. Stratmann, O. Yazyev, J. A. Austin, R. Cammi, C. Pomelli, J. W. Ochterski, P. Y. Ayala, K. Morokuma, G. A. Voth, P. Salvador, J. J. Dannenberg, V. G. Zakrzewski, S. Dapprich, A. D. Daniels, M. C. Strain, O. Farkas, D. K. Malick, A. D. Rabuck, K. Raghavachari, J. B. Foresman, J. V. Ortiz, Q. Cui, A. G. Baboul, S. Clifford, J. Cioslowski, B. B. Stefanov, G. Liu, A. Liashenko, P. Piskorz, I. Komaromi, R. L. Martin, D. J. Fox, T. Keith, M. A. Al-Laham, C. Y. Peng, A. Nanayakkara, M. Challacombe, P. M. W. Gill, B. Johnson, W. Chen, M. W. Wong, C. Gonzalez and J. A. Pople, *GAUSSIAN 03 (Revision E.01)*, Gaussian, Inc., Wallingford, CT, 2004.

14 (*a*) R. G. Parr and W. Yang, *Density Functional Theory of Atoms and Molecules*, Oxford University Press, Oxford, UK, 1989; (*b*) D. R. Salahub and M. C. Zerner, *The Challenge of d and f Electrons*, ACS Symposium Series 394, American Chemical Society, Washington, DC, 1989; (*c*) W. Kohn and L. J. Sham, *Phys. Rev.*, 1965, **140**, A1133–A1138; (*d*) P. Hohenberg and W. Kohn, *Phys. Rev.*, 1964, **136**, B864–B871.

15 (*a*) R. E. Stratmann, G. E. Scuseria and M. Frisch, *J. Chem. Phys.*, 1998, **109**, 8218–8224; (*b*) M. E. Casida, C. Jamoroski, K. C. Casida and D. R. Salahub, *J. Chem. Phys.*, 1998, **108**, 4439–4449; (*c*) R. Bauernschmitt, M. Haser, O. Treutler and R. Ahlrichs, *Chem. Phys. Lett.*, 1996, **256**, 454–464.

16 (*a*) A. D. Becke, *J. Chem. Phys.*, 1993, **98**, 5648–5652; (*b*) B. Miehlich, A. Savin, H. Stoll and H. Preuss, *Chem. Phys. Lett.*, 1989, **157**, 200–205; (*c*) C. Lee, W. Yang and R. G. Parr, *Phys. Rev. B: Condens. Matter*, 1988, **37**, 785–789.

17 P. J. Pulay, *Comput. Chem.*, 1982, **3**, 556.

18 H. B. Schlegel and J. J. McDouall, in *Computational Advances in Organic Chemistry*, ed. C. Ogretir and I. G. Csizmadia, Kluwer Academic, The Netherlands, 1991, pp. 167–185.

19 (*a*) P. J. Hay and W. R. Wadt, *J. Chem. Phys.*, 1985, **82**, 270; (*b*) W. R. Wadt and P. J. Hay, *J. Chem. Phys.*, 1985, **82**, 284; (*c*) P. J. Hay and W. R. Wadt, *J. Chem. Phys.*, 1985, **82**, 299.

20 (*a*) V. A. Rassolov, M. A. Ratner, J. A. Pople, P. C. Redfern and L. A. Curtiss, *J. Comput. Chem.*, 2001, **22**, 976; (*b*) M. M. Francl, W. J. Pietro, W. J. Hehre, J. S. Binkley, D. J. DeFrees, J. A. Pople and M. S. Gordon, *J. Chem. Phys.*, 1982, **77**, 3654; (*c*) P. C. Hariharan and J. A. Pople, *Mol. Phys.*, 1974, **27**, 209; (*d*) P. C. Hariharan and J. A. Pople, *Theor. Chim. Acta*, 1973, **28**, 213.

21 W. J. Hehre, R. Ditchfield and J. A. Pople, *J. Chem. Phys.*, 1972, **56**, 2257.

22 (*a*) S. Maity, S. Kundu, T. Weyhermüller and P. Ghosh, *Inorg. Chem.*, 2015, **54**, 1384–1394; (*b*) S. C. Patra, T. Weyhermüller and P. Ghosh, *Inorg. Chem.*, 2014, **53**, 2427–2440; (*c*) M. K. Biswas, S. C. Patra, A. N. Maity, S.-C. Ke, N. Das Adhikary and P. Ghosh, *Inorg. Chem.*, 2012, **51**, 6687–6699.

23 (*a*) A. V. Piskunov, I. N. Mescheryakova, G. K. Fukin, V. K. Cherkasov and G. A. Abakumov, *New J. Chem.*, 2010, **34**, 1746–1750; (*b*) A. I. Poddel'sky, V. K. Cherkasov and G. A. Abakumov, *Coord. Chem. Rev.*, 2009, **253**, 291–324; (*c*) C. Mukherjee, T. Weyhermüller, E. Bothe and P. Chaudhuri, *Inorg. Chem.*, 2008, **47**, 11620–11632; (*d*) K. J. Blackmore, J. W. Ziller and A. F. Heyduk, *Inorg. Chem.*, 2005, **44**, 5559–5561; (*e*) X. Sun, H. Chun, K. Hildenbrand, E. Bothe, T. Weyhermüller, F. Neese and K. Wieghardt, *Inorg. Chem.*, 2002, **41**, 4295–4303.

24 (*a*) E. Jayanthi, S. Kalaiselvi, V. V. Padma, N. S. P. Bhuvanesh and N. Dharmaraj, *Dalton Trans.*, 2016, **45**, 1693–1707; (*b*) A. Grupp, M. Bubrin, F. Ehret, Q. Zeng, F. Hartl, H. Kvapilová, S. Záliš and W. Kaim, *Eur. J. Inorg. Chem.*, 2014, 110–119; (*c*) S. C. Patra, A. Saha Roy, V. Manivannan, T. Weyhermüller and P. Ghosh, *Dalton Trans.*, 2014, **43**, 13731–13741; (*d*) L.-Z. Sui, W.-W. Yang, C.-J. Yao, H.-Y. Xie and Y.-W. Zhong, *Inorg. Chem.*, 2012, **51**, 1590–1598.

25 (*a*) R. G. Hicks, *Stable Radicals: Fundamentals and Applied Aspects of Odd-Electron Compounds*, John Wiley & Sons, Wiltshire, 2010; (*b*) F. Gerson and W. Huber, *Electron Spin Resonance of Organic Radicals*, Wiley-VCH, Weinheim, Germany, 2003.

26 (*a*) V. Vatanen, J. M. Eloranta and M. Vuolle, *Magn. Reson. Chem.*, 1999, **37**, 774–780; (*b*) R. Mäkelä and M. Vuolle, *J. Chem. Soc., Faraday Trans.*, 1990, **86**, 2569–2573.